Whole-brain functional imaging at cellular resolution using light-sheet microscopy

Misha B. Ahrens[1,*] Michael B. Orger[2], Drew N. Robson[3], Jennifer M. Li[3] and Philipp J. Keller[1,*]

[1]*Howard Hughes Medical Institute, Janelia Farm Research Campus*
[2]*Champalimaud Neuroscience Programme, Champalimaud Centre for the Unknown*
[3]*Department of Molecular and Cellular Biology, Harvard University*

[*]*Correspondence: ahrensm@janelia.hhmi.org (M.B.A.), kellerp@janelia.hhmi.org (P.J.K.)*

Supplementary Information

Supplementary Figures

Supplementary Figure 1	Physical coverage and image contrast in light sheet-based whole-brain recordings
Supplementary Figure 2	Temporal resolution of light sheet-based whole-brain recordings
Supplementary Figure 3	The hindbrain oscillator and hindbrain-spinal network in two additional brains
Supplementary Figure 4	Controls for manual selection and retina excitation artifacts
Supplementary Figure 5	Consistency of identified circuits over time

Supplementary Tables

Supplementary Table 1	Components of the light-sheet microscope for fast functional imaging

Supplementary Notes

Supplementary Note 1	Discussion of spatial and temporal resolution in other imaging scenarios
Supplementary Note 2	Analysis of movements arising from specimen drift or muscle contractions

Supplementary Software

Supplementary Software	Image processing and analysis of whole-brain functional recordings

Nature Methods: doi:10.1038/nmeth.2434

Supplementary Figure 1 | Physical coverage and image contrast in light sheet-based whole-brain recordings

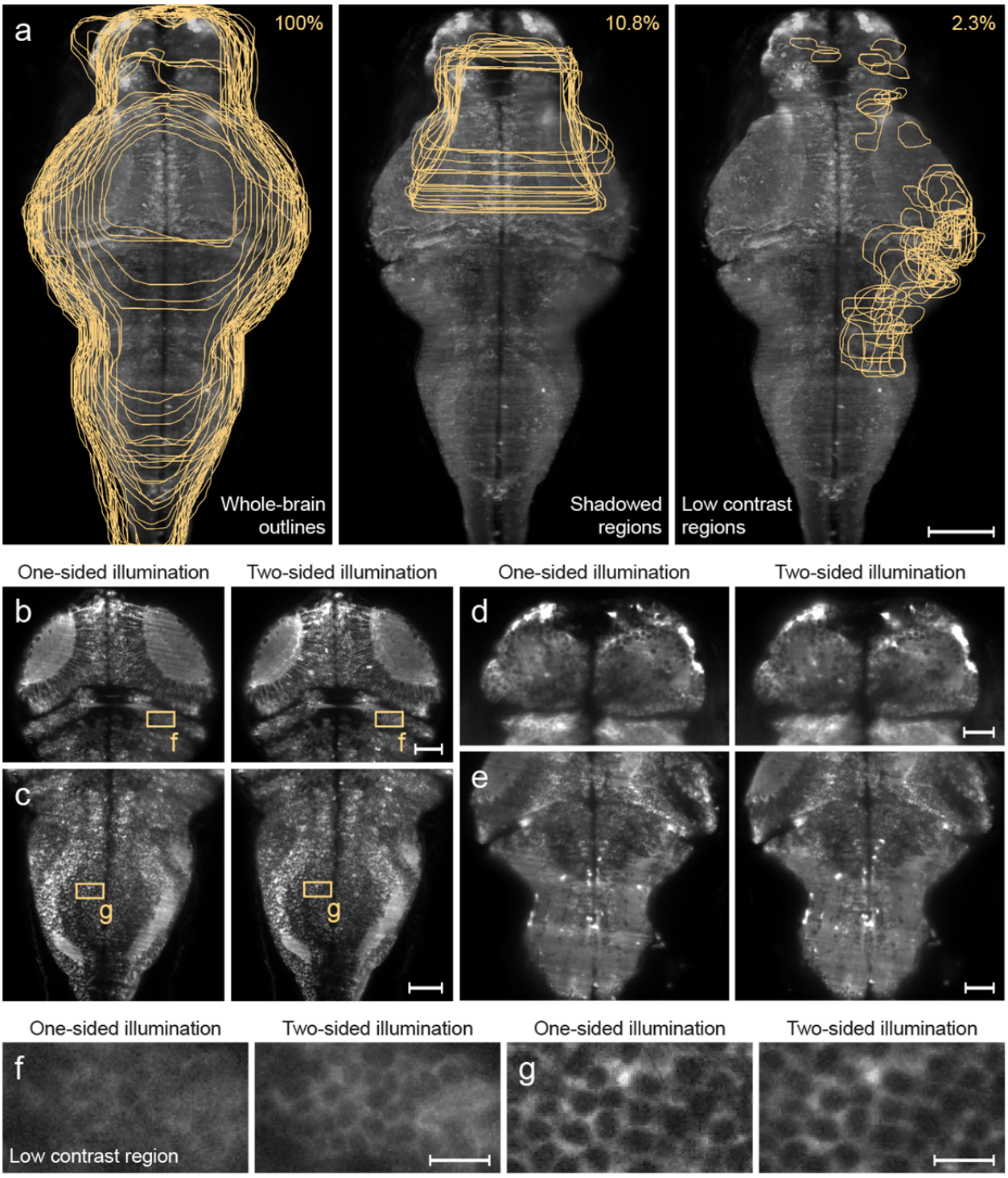

Nature Methods: doi:10.1038/nmeth.2434

Supplementary Figure 1 | Physical coverage and image contrast in light sheet-based whole-brain recordings

(**a**) *Left*: dorsal projection of whole-brain image stack (grey), obtained with one-sided light sheet illumination and superimposed with slice-based outlines of brain anatomy (orange) for all 41 slices in the volumetric data set. *Middle*: dorsal projection of whole-brain image stack (grey), superimposed with slice-based outlines of brain regions that appear in low contrast due to shadowing between the eyes. Shadowing occurs in sub-regions of 17 out of 41 slices, corresponding to 10.8% of the total recorded brain volume shown in the left panel. Although functional activity can still be recorded for these regions, image quality is insufficient for single-neuron resolution. *Right*: dorsal projection of whole-brain image stack (grey), superimposed with slice-based outlines of brain regions that appear in low contrast due to light scattering or refraction of the light sheet at the specimen surface. These sub-regions occur in 24 out of 41 slices, corresponding to 2.3% of the total recorded brain volume shown in the left panel. Although functional activity can still be recorded for these regions, image quality is insufficient for single-neuron resolution.

(**b-e**) Comparison of image quality obtained with one-sided illumination versus simultaneous two-sided illumination for different parts of the brain. The orange bounding box indicated in (b) corresponds to one of the low-contrast region marked in the right panel of (a), for which simultaneous two-sided illumination recovers single-neuron information. Another location, which is captured in higher contrast with one-sided illumination than with simultaneous two-sided illumination, is highlighted in (c). Overall differences in image quality obtained with one-sided and simultaneous two-sided illumination are small, owing to the high transparency of zebrafish larvae.

(**f**) Enlarged view of the region highlighted by the orange bounding box in (b).

(**g**) Enlarged view of the region highlighted by the orange bounding box in (c).

Scale-bars: 100 µm (a), 50 µm (b,c,e), 30 µm (d), 10 µm (f,g).

Nature Methods: doi:10.1038/nmeth.2434

Supplementary Figure 2 | Temporal resolution of light sheet-based whole-brain recordings

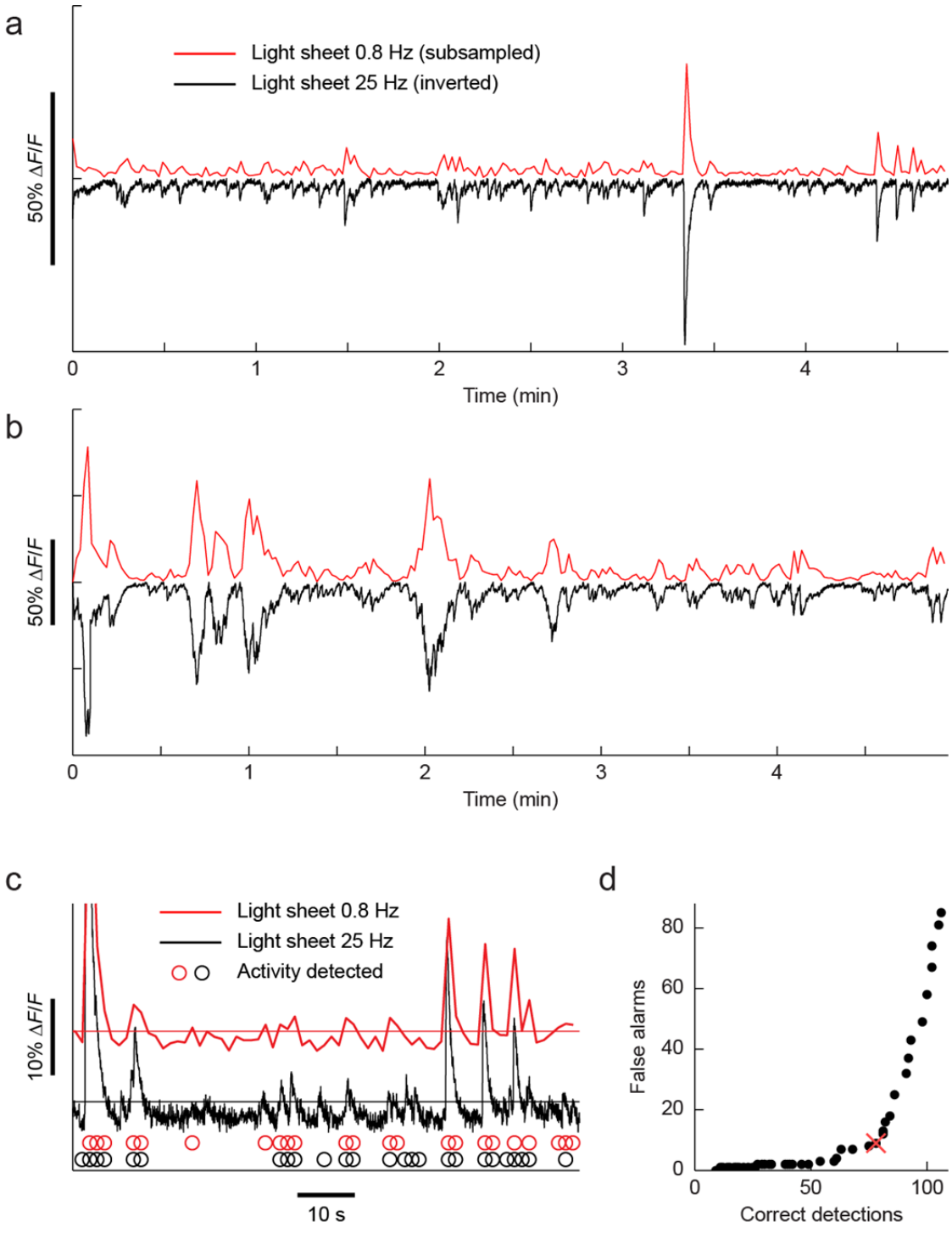

Nature Methods: doi:10.1038/nmeth.2434

Supplementary Figure 2 | Temporal resolution of light sheet-based whole-brain recordings

(**a**) In the current implementation of whole-brain functional imaging, activity of each neuron in the brain is measured once every 1.3 s. To examine which types of neural events are captured and which are missed by this sampling rate, we restricted the light sheet to one z-plane and imaged neural activity at high speed (25 Hz), yielding a measurement of activity in thousands of neurons probably with near single-spike resolution (*black trace* shows activity in one neuron). Subsampling this signal to 0.8 Hz produces the activity trace that would have been obtained with volumetric whole-brain imaging (*red trace*).

(**b**) Similar data as (a), but for a section of neuropil in the left inferior olive, of spatial extent 5 x 20 μm^2.

(**c**) To compare the degree of signal detection in a 0.8 Hz optical recording of neuronal activity, we recorded a single plane at 25 Hz (black). In this high-speed recording, it appeared possible to detect the occurrence of single-spike or bursting activity by eye. We thus assumed this data set to contain ground-truth information about spiking activity. Manually setting a threshold (black horizontal line) allowed for approximate detection of single- or multi-spike locations (black circles). To compare the fidelity of detecting such activity with the 0.8 Hz subsampled trace, we applied a variable threshold (red horizontal line represents one example) and compared the times of threshold crossing (red circles) to those of the 25 Hz signal. Low thresholds lead to larger numbers of detected events, but also to larger numbers of false alarms (detecting activity when there is none); this tradeoff is shown in panel (d).

(**d**) Number of false alarms versus correct detections, representing different threshold settings for the trace shown in panel (c). Red cross indicates the threshold indicated in (c), achieving 78 out of 106 correct detections, and 9 false alarms.

Nature Methods: doi:10.1038/nmeth.2434

Supplementary Figure 3 | The hindbrain oscillator and hindbrain-spinal network in two additional brains

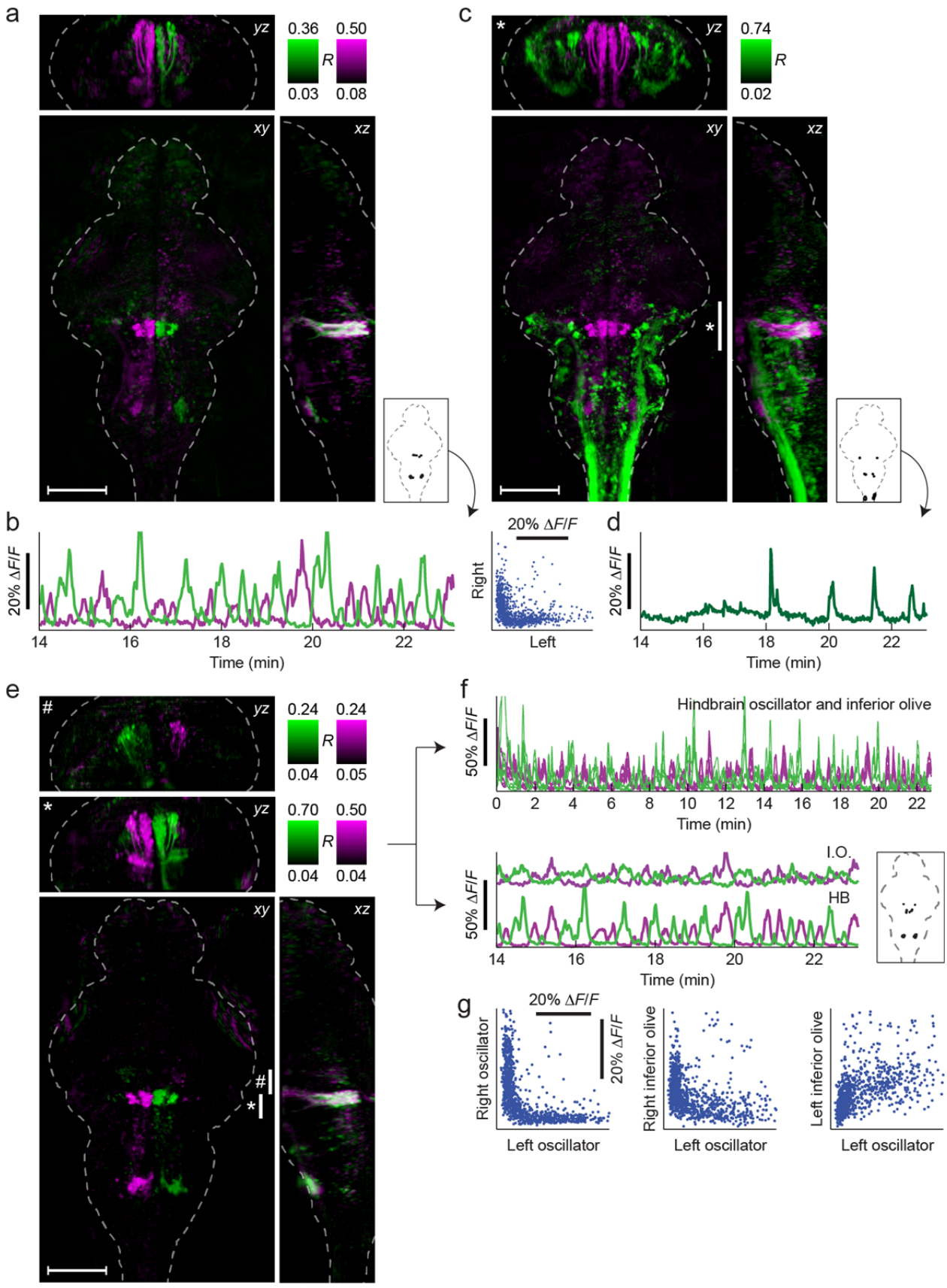

Nature Methods: doi:10.1038/nmeth.2434

Supplementary Figure 3 | The hindbrain oscillator and hindbrain-spinal network in two additional brains

Confirmation of circuit identification for hindbrain oscillator and hindbrain-spinal network in two additional larval fish brains. Panels (a-d) represent one brain, panels (e-g) another.

(**a**) Anatomy of hindbrain oscillator, visualized as maximum-intensity projections of voxels positively (green) and negatively (magenta) correlated to the corresponding reference trace. *Top*: front projection, *bottom*: top projection, *right*: side projection.

(**b**) *Left:* fluorescence signals, averaged over left and right groups of neurons indicated in the map in the bottom-right corner of panel (a). *Right:* same data shown as a scatter plot, illustrating anticorrelation between the left and right halves of the hindbrain oscillator.

(**c**) The spinal-hindbrain network, in the same fish, derived from the same time-lapse recording. Magenta: populations from (a), green: correlation to a second functional trace.

(**d**) Fluorescence signal averaged over the population indicated in the map in the bottom-right corner of panel (c).

(**e**) The hindbrain oscillator in a second fish brain. *Top:* Anterior to the hindbrain oscillator are populations with flipped polarity, with the left (right) population correlating to the right (left) part of the hindbrain oscillator. Location indicated by "#" in bottom panel. These populations were detectable in two other fish.

(**f**) Individual activity traces (*top*) and averages (*bottom*) of neurons indicated in the map in the bottom-right corner.

(**g**) Scatter plots of data shown in panel (f), *bottom*.

Scale-bars: 100 μm (a,c,e).

Nature Methods: doi:10.1038/nmeth.2434

Supplementary Figure 4 | Controls for manual selection and retina excitation artifacts

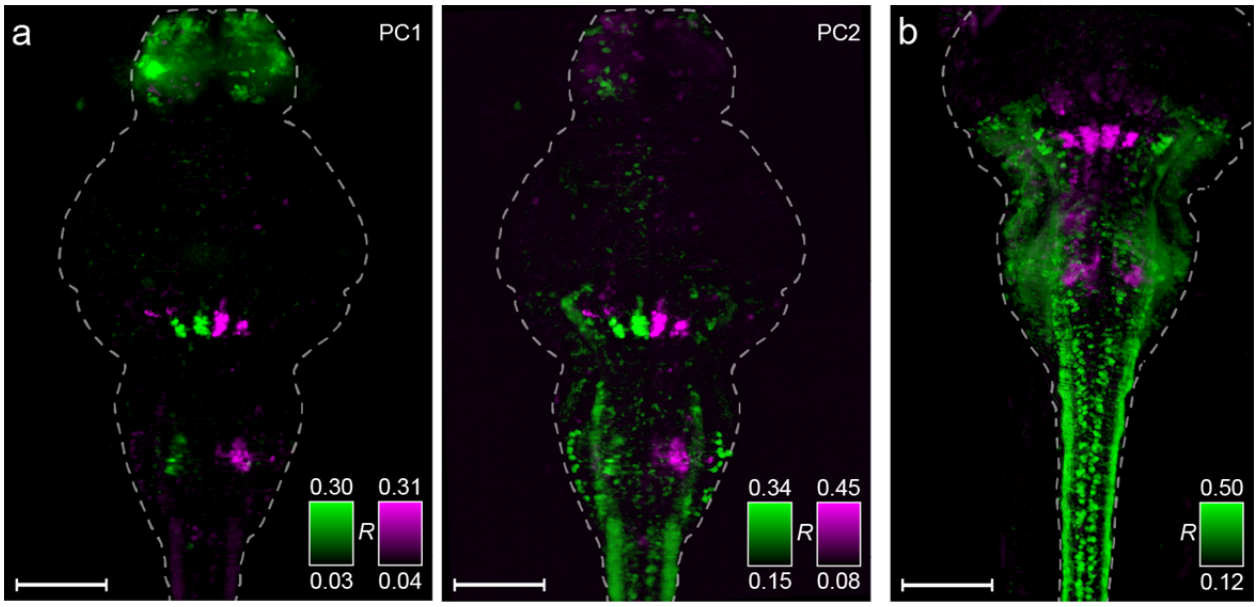

Nature Methods: doi:10.1038/nmeth.2434

Supplementary Figure 4 | Controls for manual selection and retina excitation artifacts

(**a**) Functionally-defined neuronal populations after replacing the manual step of the analysis (**Figure 4c**) by Principal Components Analysis (PCA). Correlating whole-brain signals to the PCA-defined reference signals yields populations similar to those obtained using the manual step, but results are more intermixed (analysis is based on the same brain as **Figure 6**). The first principal component, PC1, yields a mixture of the hindbrain oscillator (green, magenta), the hindbrain-spinal network (faint magenta) and tissue in the forebrain (green). PC2 yields a mixture of the hindbrain oscillator (green, magenta) and the spinal-hindbrain network (green). This has two implications: First, PCA is not superior to manual selection for detecting functionally related sets of neurons. Second, a fully automated analysis using PCA produces similar results as the analysis with the manual step, ruling out human bias in selecting for anatomical structure.

(**b**) Identification of the hindbrain oscillator and the hindbrain-spinal network in a fish, whose eyes, forebrain and midbrain were excluded from direct exposure to the illuminating blue laser light (analysis is based on the same brain as **Supplementary Figure 3e**). Anatomical and functional properties are the same, and therefore do not arise from excitation of the photoreceptors by direct exposure to the laser beam.

Scale-bars: 100 μm (a,b).

Nature Methods: doi:10.1038/nmeth.2434

Supplementary Figure 5 | Consistency of identified circuits over time

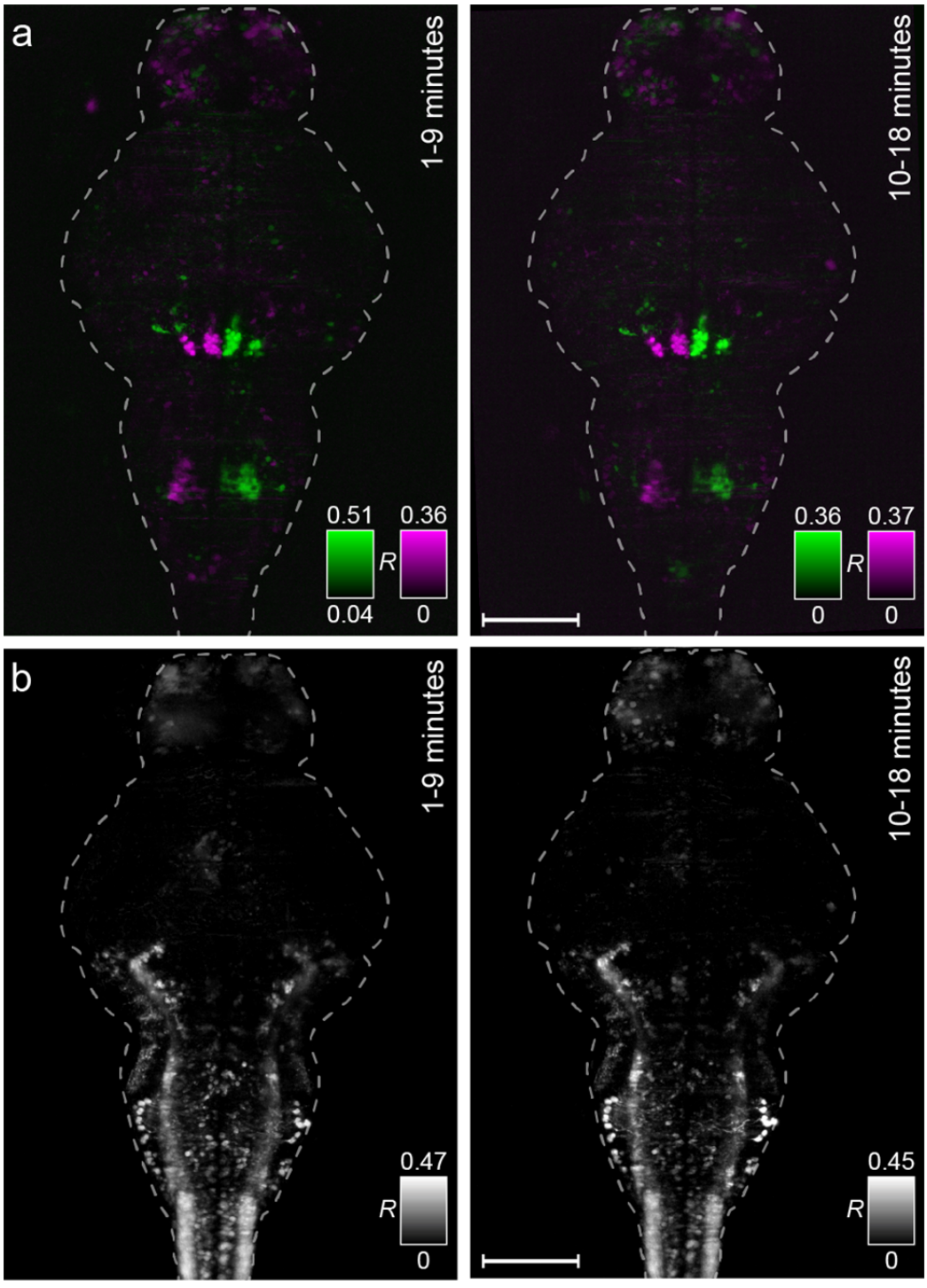

Nature Methods: doi:10.1038/nmeth.2434

Supplementary Figure 5 | Consistency of identified circuits over time

(**a**) To examine whether the anatomical structures identified by the semi-automatic analysis method are consistent over time, we performed the analysis separately for the first and second halves of an ~18 min data set (obtained from an ~22 min recording, with the first ~4 min discarded to remove transient effects of the initiation of the experiment; depicted is the fish from **Figure 6**). The two recovered neuronal populations are almost identical. This implies that the structure of this hindbrain oscillator does not change over the time course of the experiment, supporting the notion that this is indeed a consistent functional circuit.

(**b**) The same analysis as in (a) applied to the hindbrain-spinal network. This functional circuit is also stable over the duration of the experiment.

Scale-bars: 100 μm (a,b).

Nature Methods: doi:10.1038/nmeth.2434

Supplementary Table 1 | Components of the light-sheet microscope for fast functional imaging

Module	Component	Product(s)	Manufacturer
Lasers (shared module)	SOLE-3 module	Solid-state laser: 488 nm DPSS lasers: 561/594 nm	Omicron Laserage
Illumination systems (two mirrored modules)	High-speed laser shutter	VS14S2ZM1-100 with AlMgF2 coating VMM-D3 three-channel driver	Uniblitz
	Illumination filter wheel	96A351 filter wheel MAC6000 DC servo controller	Ludl
		NDQ neutral density filters	Melles Griot
	Miniature piezo tip/tilt mirror	S-334 tip/tilt mirror E-503.00S amplifier E-509.S3 servo controller E-500 chassis	Physik Instrumente
	F-theta lens	66-S80-30T-488-1100nm custom lens	Special Optics
	Tube lens module	U-TLU-1-2 camera tube	Olympus
	Piezo objective positioner	P-622.1CD PIHera piezo stage E-665 piezo amplifier and servo controller	Physik Instrumente
	Illumination objective	XLFLUOR 4x/340/0.28	Olympus
Detection system	Piezo objective positioner	P-622.1CD PIHera piezo stage E-665 piezo amplifier and servo controller	Physik Instrumente
	Detection objective	CFI75 LWD 16xW/0.8 water-dipping objective	Nikon
		Plan-Apochromat 20x/1.0 water-dipping objective	Carl Zeiss
	Detection filter wheel	96A354 filter wheel MAC6000 DC servo controller	Ludl
		RazorEdge long-pass filters 525/50 BrightLine band-pass filter	Semrock

Nature Methods: doi:10.1038/nmeth.2434

Supplementary Table 1 (continued)

Module	Component	Product(s)	Manufacturer
Detection system	Tube lens module	CFI second lens unit	Nikon
		AxioImager 130 mm ISD tube lens	Carl Zeiss
	Camera	Orca Flash 4.0	Hamamatsu
Specimen chamber	Specimen chamber	Scaffold manufactured from black Delrin	Custom design
	Specimen holder	Holder manufactured from medical-grade stainless steel Multi-stage adapter module for connecting to specimen positioning system	Custom design
Specimen positioning system	Customized translation stages (three units)	M-111K046	Physik Instrumente
	Rotary stage	M-116	Physik Instrumente
	Motion I/O interface and amplifier	C-809.40 4-channel servo-amplifier	Physik Instrumente
	Motion controller	PXI-7354 4-axis stepper/servo motion controller	National Instruments
Real-time electronics	Real-time controller with LabVIEW Real-Time OS	PXI-8110 Core 2 Quad 2.2 GHz	National Instruments
	I/O interface boards (three units)	PXI-6733 high-speed analog output 8-channel board	National Instruments
	BNC connector boxes (three units)	BNC-2110 shielded connector block	National Instruments
	Serial interface board	PXI-8432/2	National Instruments
	Summing amplifier	SIM900 mainframe 4x SIM980 analog summing amplifiers	Stanford Research Systems

Nature Methods: doi:10.1038/nmeth.2434

Supplementary Table 1 (continued)

Module	Component	Product(s)	Manufacturer
Control software	Real-time modules	32-bit LabVIEW code	Custom software
	Host modules	64-bit LabVIEW code	Custom software
Workstations and servers	Data acquisition workstation	2x X5680 HexaCore CPUs	Intel Corporation
		18x 8 GB DDR-3 RAM modules	Kingston
		24-channel RAID controller 52445	Adaptec
		24x Cheetah 15K.7 SAS-2 600GB hard disks	Seagate
		10 Gigabit fiber network adapter EXPX9501AFXSR	Intel Corporation
		GeForce GTX470 graphics card	Nvidia Corporation
		2x Full-Configuration CameraLink frame grabbers	Hamamatsu
		X8DAH+-F server board	Supermicro
	Fiber network-attached storage server	S5520SC-based standard rack-mount server	Intel Corporation
	Fiber network-attached RAID system	CX4260-X4 4U rack-mount server	Colfax
		36x Ultrastar A7K4000 SATA-2 4TB hard disks	Hitachi

Nature Methods: doi:10.1038/nmeth.2434

Supplementary Note 1 | Discussion of spatial and temporal resolution in other imaging scenarios

In addition to our experimental characterization of the whole-brain functional imaging experiments in the larval zebrafish brain (**Online Methods**), we provide a brief discussion of expected performance of our functional imaging method in two additional imaging scenarios: (1) a smaller volume corresponding to the size of the *Drosophila* embryonic ventral nerve cord, and (2) a larger volume covering half a cubic millimeter.

In the first scenario, a block volume of the size 350 x 85 x 50 μm^3 is imaged with a single light sheet, using a Nikon 25x/1.1 water-dipping objective for detection and a PI P-622.1CD Hera stage for objective positioning. Assuming that the microscope is equipped with a Hamamatsu Orca Flash 4.0 camera (6.5 μm pixel pitch) and aligned using the Rayleigh criterion (light sheet thickness at the edge of the field-of-view is by square root of 2 larger than at the center), a light sheet thickness of 3.01 ± 0.33 μm (FWHM, mean ± s.d.) across the field of view and an effective lateral resolution of 0.52 μm (twice the pixel size, owing to spatial under-sampling) are expected. By scanning this volume in steps of 3.13 μm (17 planes) at a frame rate of 31 Hz, a temporal resolution of 0.5 s can be achieved.

In the second scenario, a block volume of the size 1,000 x 1,000 x 500 μm^3 is imaged with two light sheets, using a Carl Zeiss 10x/0.45 water-dipping objective for detection and a PI P-625.1CD Hera stage for objective positioning. Assuming that the microscope is equipped with a Hamamatsu Orca Flash 4.0 camera and aligned using the Rayleigh criterion, a light sheet thickness of 6.53 ± 0.72 μm (FWHM, mean ± s.d.) across the field of view and an effective lateral resolution of 1.3 μm (twice the pixel size, owing to spatial under-sampling) are expected. By scanning this volume in steps of 7 μm (72 planes) at a frame rate of 31 Hz, a temporal resolution of 2.3 s can be achieved.

Nature Methods: doi:10.1038/nmeth.2434

Supplementary Note 2 | Analysis of movements arising from specimen drift or muscle contractions

We analyzed the magnitude of movements related to specimen drift, heartbeat and other types of muscle contractions, in order to estimate their potential impact on the correlation analyses of time-varying functional activity in the whole-brain recordings.

First, we analyzed high-speed light-sheet recordings of individual planes at different depths in the brain. These sub-regions were recorded at 25 Hz. Within the limits of the measurement sensitivity provided by the spatial sampling in these recordings, we did not observe movement artifacts related to heartbeat.

Second, we analyzed the amount of global specimen drift over the observation period. The drift was determined manually on the single-cell level by measuring lateral and axial displacement vectors in interpolated image stacks with respect to a reference stack. Over a recording period of 2,000 time points (40-45 min), we measured an average lateral drift (along *x*- and *y*-axis) of 2.02 ± 0.47 µm (mean ± s.d., $n = 15$) and an average dorso-ventral drift (along *z*-axis) of 1.43 ± 0.62 µm (mean ± s.d., $n = 10$). In the post-processing pipeline, the lateral component of this global drift is compensated by the spatial registration procedure. However, this procedure does not consider the axial drift component. Thus, the average uncorrected global spatial drift of the brain is on the order of $1/5^{th}$ of the average diameter of a cell body (or $1/3^{rd}$ of the *z*-step size) over a course of 40-45 min.

Although our cellular-resolution analyses of brain activity are not significantly affected by movement arising from heartbeat and long-term drift, other types of muscle contractions constitute a possible third source of movement artifacts. Large-scale contractions are easily detectable by inspecting the dorsal, lateral and frontal maximum-intensity projections of the recorded data sets. The analyses presented in this manuscript are based on recordings with a minimal amount of such contractions (less than one contraction per 15 min), as determined by manual inspection. Smaller, local tissue contractions can occur and are occasionally visible, for example, in dorsal hindbrain regions of the 40 and 50 µm deep planes in **Supplementary Video 2**. We measured the maximum short-term and maximum long-term local displacements resulting from such deformations, using the same measurement approach as above. For short-term

Nature Methods: doi:10.1038/nmeth.2434

displacements (adjacent frames), we obtained a maximum lateral distance of 1.53 ± 0.41 μm (mean ± s.d., n = 20) and a maximum axial distance of 0.40 ± 0.31 μm (mean ± s.d., n = 10). For long-term displacements, we obtained a maximum lateral distance of 7.00 ± 1.85 μm (mean ± s.d., n = 20) and a maximum axial distance of 1.72 ± 0.48 μm (mean ± s.d., n = 10). In contrast to the almost isotropic global drift discussed above, local tissue contractions thus appear to result in displacements that are less pronounced along the dorso-ventral body axis. Also in this case only the lateral component is compensated by the local registration procedure in the post-processing pipeline. The maximum uncorrected displacements arising from local tissue contractions are thus on the order of $1/4^{th}$ of the average diameter of a cell body for long-term displacements. We note that only a small fraction of all cells is subject to this type of movement, and the value reported here represents the estimated maximum displacement based on this pool of cells.

Nature Methods: doi:10.1038/nmeth.2434

Supplementary Software | Image processing and analysis of whole-brain functional recordings

This software package contains custom tools for registration, Δ*F*/*F* calculation and analysis of high-speed light-sheet microscopy recordings of zebrafish larval brains expressing a genetically-encoded calcium indicator. All algorithms were developed using the Matlab computer language (version R2012b, The Mathworks). In addition to the Matlab core installation, the Parallel Computing Toolbox is recommended for multi-threaded execution of the code. Software compatibility was only verified for PCs with a Windows 7 64-bit operating system.

Software modules (listed in the order of their application):

- **runRegistration.m**

  Note: This program performs non-linear spatial registration of a raw whole-brain time-lapse microscopy data set, using a pre-defined reference time interval. The script enables multi-threaded execution of this task, allowing up to 12 parallel threads. Execution requires the auxiliary functions *registerImages.m*, *registerStacks.m* and *warpImages.m*.

- **createReference.m**

  Note: This program operates on the registered time-lapse microscopy data set and generates the volumetric reference stacks required for Δ*F/F* calculation. The reference stacks are obtained by using a spatial median filter and temporal percentile computation based on a sliding-window approach. The script enables multi-threaded execution of this task, allowing up to 12 parallel threads.

- **extractSignal.m**

  Note: This program operates on the registered time-lapse microscopy data set and performs the volumetric Δ*F*/*F* calculation, using the reference stacks generated by *createReference.m*. The script enables multi-threaded execution of this task, allowing up to 12 parallel threads.

- **selectTrace.m**

  Note: This program operates on the fluorescence traces in super-voxel representation, which are extracted from the Δ*F*/*F* stacks generated by *extractSignal.m*, and performs fluorescence trace ranking based on the power spectrum to generate a correlation matrix of the best hits

Nature Methods: doi:10.1038/nmeth.2434

for a pre-defined frequency range. Using the graphical user interface of *selectTrace.m*, individual voxels can be selected from this correlation matrix to determine a functional anatomy preview of highly correlated or anti-correlated fluorescence traces.

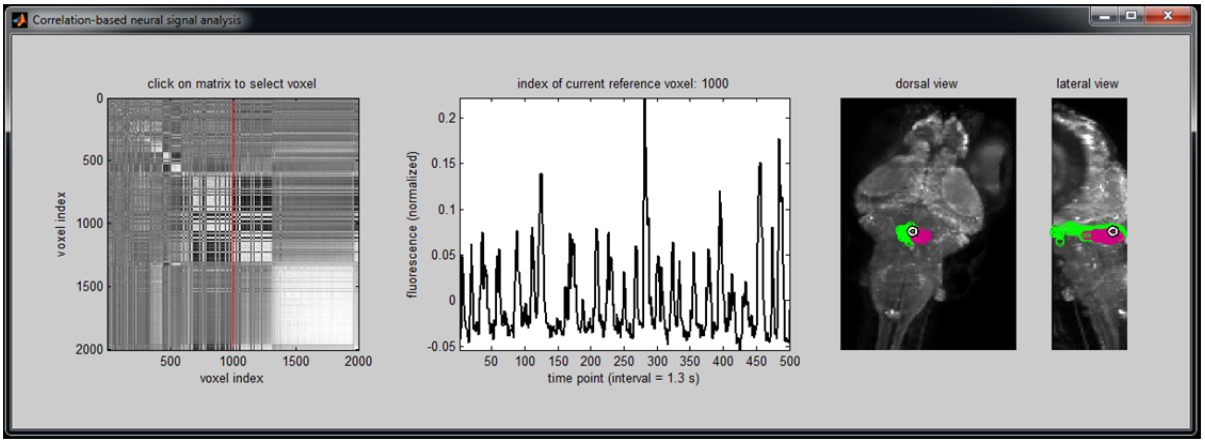

Screenshot of the graphical user interface of *selectTrace.m*

- **makeReferenceMontage.m**

  Note: This program generates a scaled multi-slice visualization of the reference stacks computed by *createReference.m*, which is used together with the output of *makeMontage.m* to inspect and present the functional activity information captured in the whole-brain time-lapse recordings (see **Supplementary Video 3**). The script enables multi-threaded execution of this task, allowing up to 12 parallel threads.

- **makeMontage.m**

  Note: This program generates a scaled multi-slice visualization of the $\Delta F/F$ stacks computed by *extractSignal.m*, which is used together with the output of *makeReferenceMontage.m* to inspect and present the functional activity information captured in the whole-brain time-lapse recordings (see **Supplementary Video 3**). The script enables multi-threaded execution of this task, allowing up to 12 parallel threads.

- **rotateReferenceMIP.m**

  Note: This program generates a projection-based visualization of the reference stacks computed by *createReference.m*, which is used together with the output of *rotateMIP.m* to inspect and present the functional activity information captured in the whole-brain time-lapse

Nature Methods: doi:10.1038/nmeth.2434

recordings (see **Supplementary Video 4**). The script enables multi-threaded execution of this task, allowing up to 12 parallel threads.

- **rotateMIP.m**

  Note: This program generates a projection-based visualization of the Δ*F*/*F* stacks computed by *extractSignal.m*, which is used together with the output of *rotateReferenceMIP.m* to inspect and present the functional activity information captured in the whole-brain time-lapse recordings (see **Supplementary Video 4**). The script enables multi-threaded execution of this task, allowing up to 12 parallel threads.

Input data structure:

The first computational module of the pipeline (*runRegistration.m*) expects raw input data to be provided as 3D image stacks in TIF format, using the following naming scheme and directory structure (*ttttt* = time point, *x* = camera index):

[Root]/SPM00/TM*ttttt*/ANG000/SPC00_TM*ttttt*_ANG000_CM*x*_CHN00_PH0.tif

Nature Methods: doi:10.1038/nmeth.2434